

# Spectroscopic (XANES/XRF) characterization of contaminant manganese cycling in a temperate watershed

Elizabeth M. Herndon · Carmen E. Martínez · Susan L. Brantley

Received: 8 April 2014 / Accepted: 22 July 2014  
© Springer International Publishing Switzerland 2014

**Abstract** Many soils around the globe are contaminated with metals due to inputs from anthropogenic activities; however, the long-term processes that retain these metals in soils or flush them into river systems remain unclear. Soils at the Susquehanna/Shale Hills Critical Zone Observatory, a headwater catchment in central Pennsylvania, USA, are enriched in manganese due to past atmospheric deposition from industrial sources. To investigate how Mn is retained in the catchment, we evaluated the spatial distribution and speciation of Mn in the soil–plant system using X-ray fluorescence and X-ray Absorption Near Edge Structure spectroscopies. Weathered soils near the land surface were enriched in both amorphous and crystalline

Mn(III/IV)-oxides, presumably derived from biogenic precipitation and atmospheric deposition, respectively. In contrast, mineral soils near the soil–bedrock interface contained Mn(II) in clays and crystalline Mn(III/IV)-oxides that formed as Mn(II) was leached from the parent shale and oxidized. Roots, stems, and foliar tissue were dominated by organic-bound and aqueous Mn(II); however, a small portion of foliar Mn was concentrated as organic-bound Mn(III) in dark spots that denote Mn toxicity. During decomposition of leaves and roots, soluble Mn(II) stored in vegetation was rapidly oxidized and immobilized as mixed-valence Mn-oxides. We propose that considerable uptake of Mn by certain plant species combined with rapid oxidation of Mn during organic matter decomposition contributes to long-term retention in soils and may slow removal of Mn contamination from watersheds.

Responsible Editor: James Sickman

**Electronic supplementary material** The online version of this article (doi:10.1007/s10533-014-0018-7) contains supplementary material, which is available to authorized users.

E. M. Herndon · S. L. Brantley  
Department of Geosciences, The Pennsylvania State University, University Park, PA 16802, USA

E. M. Herndon (✉)  
Department of Geology, Kent State University, Kent, OH 44242, USA  
e-mail: eherndo1@kent.edu

C. E. Martínez  
Department of Crop and Soil Sciences, Cornell University, Ithaca, NY 14853, USA

**Keywords** Manganese · Spectroscopy · Critical zone · Soil geochemistry · Metal contamination

## Introduction

Manganese (Mn) is a highly reactive component of soils and plays a central role in contaminant transport, redox reactions, and the breakdown of soil organic matter (Suarez and Langmuir 1976; Hofrichter 2002; Berg et al. 2007). Although considered a trace element, it is generally present at concentrations of 350–2,000 ppm in soils and 30–300 ppm in leaf tissue (Kabata-Pendias

and Pendias 2001), making it one of the most abundant trace metals in soils and plants. Anthropogenic endeavors such as steel production and coal combustion have led to the enrichment of Mn in soils, water, and biota throughout the globe (Nriagu and Pacyna 1988; Pacyna and Pacyna 2001; Herndon et al. 2011). In order to understand the long-term retention of contaminant Mn in soils and transport from soils into water systems, it is necessary to examine the factors that influence Mn mobility in watersheds.

Biological factors, including microbially-mediated redox reactions and uptake into vegetation, can have a large influence on Mn mobility. Plants take up dissolved Mn(II) from soil pore waters and store it in foliar tissue as free or carboxylate-bound Mn(II) (e.g. bound to citrate, oxalate, malate) (Xu et al. 2009; Fernando et al. 2010; White 2012). Excess Mn in leaf tissue increases oxidative stress and leads to Mn toxicity (Gonzalez and Lynch 1999; St. Clair et al. 2005). Although Mn distribution and speciation in plant tissues varies widely amongst species, black spots on foliage are primary indicators of Mn toxicity (Blamey et al. 1986; Horiguchi 1987; McNear et al. 2005; Broadhurst et al. 2009). These spots are enriched in Mn and have been proposed to predominantly contain either reduced Mn(II) (Broadhurst et al. 2009) or oxidized Mn and polyphenols (Horiguchi 1987; McNear and Kupper 2014).

Fungi and bacteria catalyze the kinetically-slow oxidation of soluble Mn(II) to generate Mn(III)-ligand complexes and insoluble phyllo-manganates in the environment (Schulze et al. 1995; Hofrichter 2002; Bargar et al. 2005; Webb et al. 2005; Miyata et al. 2006; Santelli et al. 2011). A variety of fungal species are able to oxidize Mn(II) to a nanoparticulate, hexagonal birnessite phase (Santelli et al. 2011), similar to that previously characterized as a product of bacterial Mn oxidation (Bargar et al. 2005; Webb et al. 2005; Learman et al. 2011a). The species-dependent conversion of hexagonal birnessite to more ordered structures (e.g. todorokite, triclinic birnessite) leads to significant variability in Mn-oxide morphology (Santelli et al. 2011) and suggests diverse biological oxidation pathways, including direct enzymatic oxidation (Webb et al. 2005; Miyata et al. 2006) or oxidation by reaction with bacterially produced superoxide (Archibald and Fridovich 1982; Learman et al. 2011b, 2013). Reactive birnessite minerals formed from biogenic Mn oxidation can catalyze subsequent abiotic Mn oxidation (Learman et al. 2011a), facilitating immobilization of soluble Mn(II) as Mn(III/IV)-oxides.

The Susquehanna/Shale Hills Critical Zone Observatory (SSHCZO) is a temperate, forested watershed located in central Pennsylvania, USA. In a detailed geochemical study at the SSHCZO, ridge top soils were found to be enriched in Mn relative to the shale bedrock (Herndon et al. 2011). Manganese concentrations were high near the soil surface and decreased with depth in the profile until reaching parent composition, consistent with an addition profile for atmospherically input elements (Brantley and Lebedeva 2011). Manganese enrichment in the soil was found to be consistent with short-term, high-magnitude atmospheric inputs from industrial deposition, likely derived from nineteenth century iron smelting and/or coal combustion which also enriched Pb in these soils (Herndon et al. 2011; Herndon 2012). Annual fluxes of Mn from soil to foliage via plant uptake and from foliage to soil via litterfall exceed leaching of Mn from the soil by two orders of magnitude (Herndon and Brantley 2011; Herndon 2012). While high rates of Mn cycling by trees can lead to high Mn concentrations in organic-rich surface soils (Horsley et al. 2000; Jobbagy and Jackson 2004; Oh and Richter 2005; Kogelmann and Sharpe 2006), the mechanisms that retain Mn in soils following litterfall are not established.

In this study, we investigated processes that sequester Mn in soils by identifying chemical transformations of Mn that occur during transport through the SSHCZO watershed. X-ray Fluorescence (XRF) and X-ray Absorption Near Edge Structure (XANES) spectroscopies were used to evaluate the spatial distribution and chemical speciation of Mn in soils, plants, and decomposing foliage. Spectroscopic data were integrated with bulk chemistry observations in order to evaluate the hypothesis that vegetation slows the removal of Mn contamination from impacted environments by taking up Mn from the soil and storing it in biomass and organic matter.

## Methods

### Sample collection

The Susquehanna Shale Hills Critical Zone Observatory (SSHCZO) located in Huntingdon Co., Pennsylvania, is one of several CZOs in the United States and has been the focus of extensive geochemical characterization (e.g. Jin et al. 2010; Ma et al. 2010; Andrews et al. 2011). A ridge top soil core was augered from the south slope of

the watershed in July 2008 (core ID: RT08). The core was collected in depth increments of 0–11 cm, 11–16 cm, and 16–22 cm, where 0 was defined as the top of the mineral soil. Point of refusal, defined as the depth in the soil at which we could no longer physically auger, was reached at 22 cm and is the best approximation for the soil–bedrock interface. Additionally, the organic horizon was collected by hand from the surface of the soil and included a mat of organic material that was pulled away from the mineral soil surface. Leaf litter was collected by hand from the soil surface. An additional mineral soil sample was collected on the same date as RT08 from a core augered in the valley floor directly downslope from the ridge core (core ID: VF08). This sample was collected at the soil–bedrock interface (62–66 cm). These soil samples were kept at field moisture conditions at 4 °C for three months until spectroscopic analysis. Three additional soil cores were collected from the ridge top in September 2007 to depths of 6.0 cm (core AR1), 17.5 cm (AR3), and 22 cm (AR2) and subsequently air-dried in the laboratory prior to chemical extractions.

Upper-canopy leaves and stems were sampled in June 2011 from two mature *Quercus prinus* (chestnut oak) trees and one mature *Acer saccharum* (sugar maple) tree growing at the Shale Hills CZO. *Quercus* species represent >50 % of all canopy tree species at SSHCZO while *Acer* species are less abundant but more susceptible to Mn toxicity (~7 %) (Wubbels 2010; St. Clair et al. 2005). Leaves and stems were obtained by climbing the trees and using a pole cutter to remove a section of the tree branch. Additional leaf and root samples were obtained from underbrush seedlings at SSHCZO in September 2008 and from greenhouse-grown *Q. rubra* (red oak) seedlings in July 2011. The red oak seedlings were used in a complimentary study to quantify Mn uptake into vegetation and leaching from mineral soil (Herndon 2012).

## Laboratory methods

### *Wet chemistry techniques*

To determine cation concentrations, subsamples of each soil were ground to <150 µm particle size, fused with lithium metaborate at 900 °C, and dissolved in nitric acid. These solutions were analyzed on inductively coupled plasma atomic emission spectroscopy (ICP-AES) at Penn State’s Materials Characterization Laboratory. Leaf subsamples were dried, ground in

liquid nitrogen, and chemically analyzed on ICP-AES following ashing and acid dissolution at Penn State’s Agricultural Analytical Services Laboratory.

Subsamples from ridgetop soil cores (AR1, AR2, and AR3) were sieved to obtain sand (63–2,000 µm) and coarse silt (38–63 µm) size fractions. Each size fraction was sequentially extracted with 1.0 M ammonium acetate, 0.5 M hydrochloric acid, and 0.3 M sodium dithionite to leach Mn contained in exchangeable (EXCH), amorphous oxide (AMOR), and crystalline oxide (OXIDE) fractions, respectively (Kostka and Luther, 1994; Zemberyova et al., 1998). Cation concentrations in the extract solutions were analyzed on ICP-AES. The residual material (RES) remaining after the three-step extraction procedure, assumed to contain mostly silicate minerals, was analyzed on ICP-AES following lithium metaborate fusion.

### *Litter decomposition*

Leaves and roots from underbrush seedlings were analyzed with XANES spectroscopy while fresh and then after 6 months of decomposition. Decomposition was performed in closed vessels in the laboratory, and the samples exhibited visual growth of microbial biomass. A complimentary decomposition study was performed by burying leaf litter in soils for approximately 2 months. Microporous specimen capsules (78 µm porosity; Electron Microscopy Sciences), i.e. “wells”, were packed with crushed leaf litter and buried 10 cm deep in oxic soils in either SSHCZO ridge soils (7 weeks) or in mineral soils containing red oak seedlings in the greenhouse (9 weeks). The pore size of the capsules was selected to inhibit root penetration while allowing exchange of water and microbial biomass.

### *Preparation for spectroscopic analysis*

For bulk XANES analyses, fresh vegetation samples were ground in liquid nitrogen with a mortar and pestle and stored as a powder until analysis. For XRF maps and µXANES spot analysis, intact fresh leaves were vacuum-sealed in bags and stored frozen for <1 month until just prior to analysis. Fresh roots and stems were sectioned with a box cutter, vacuum-sealed, and frozen. Fine roots could not be sectioned fresh due to their size; therefore, we embedded these roots in LR White Hard Grade acrylic resin embedding medium (#14383; Electron Microscopy Sciences) using methods adapted

from Tippkötter and Ritz (1996), Nunan et al. (2001), and Eickhorst and Tippkötter (2008). Briefly, the fine roots were cut into small segments, fixed with 3 % paraformaldehyde, and dehydrated in ethanol prior embedding in the resin and curing at 65 °C. Once the resin fully polymerized (3–5 days), a box cutter was used to slice 1 mm thick sections of each sample to expose cross-sections of embedded roots. A similar technique was used to preserve the buried wells after their removal from the soil. Each microporous well was submerged in sequential solutions of paraformaldehyde, ethanol, and LR White resin prior to curing in an oven at 65 °C. Embedded wells were cut into ~2 mm thick sections with a slow saw to expose cross-sections of the buried leaf litter.

## XANES and XRF spectroscopy

### *Data collection*

XRF maps and Mn K-edge XANES were obtained at the Advanced Photon Source (APS) on beamline 20-BM (XANES), 13-BM-D GSECARS (XRF/XANES) and 13-ID-C GSECARS (XRF/XANES). Beamline 20-BM operates with a bending magnet source, Si(111) monochromator, and unfocused beam (30 × 1 mm) with a flux of  $1 \times 10^{11}$  photons/s at 10 keV. Beamline 13-BM-D utilizes a bending magnet source with a  $1 \times 10^9$  flux (photons/sec) at 10 keV, a Si(111) monochromator, and a Vortex ME-4 Silicon Drift Detector. An unfocused beam (50 × 4 mm) was used for ground bulk samples and a focused beam (10 × 30 μm) was used for mapping and obtaining μXANES spectra on regions of interest. Beamline 13-ID-C utilizes an undulator source with a flux of  $1 \times 10^{13}$  photons/sec for the unfocused beam (3 × 1 mm) and  $1 \times 10^{11}$  photons/sec for the focused beam (5 × 5 μm) at 10 keV. Additional hardware included a Si(111) monochromator, a Vortex ME-4 Silicon Drift Detector, and Kirkpatrick-Baez mirrors for focusing.

Mineral standards were prepared for XANES by spreading thin layers of the powdered material on X-ray transparent Kapton tape and stacking squares of the tape to achieve transmissive samples with adequately high Mn counts. Ground soil and vegetation samples were packed into plastic sample holders and sealed with Kapton tape. Intact vegetation and well samples were secured with tape to a sample mount in the beamline hatch.

For XANES spectra, data were collected between –100 and +200–500 eV around the zero-valent Mn K-edge ( $E_0 = 6,537.7$  eV). Multiple scans were collected for each sample, and no beam damage was observed during subsequent scans. At 13-ID-C, due to the risk for beam damage under the high intensity photon flux, vegetation samples were kept in a cold stage during data collection. Bulk minerals were run in transmission mode. A fluorescence detector was used for bulk samples with low Mn concentrations (e.g. bulk vegetation, bulk soil), samples that were not transmissive (e.g. leaves, buried wells, roots and stems), and for mapping. XRF maps were collected at 10 keV with a focused beam and a step size of 5 μm (13-ID-C) or 25–40 μm (13-BM-D). Fluorescence counts for each element were averaged over the area of the pixel, and pixels with warm colors correspond to high fluorescence counts while pixels with cool colors correspond to low fluorescence counts. Here, qualitative differences in fluorescence counts within each map are presented.

### *Data processing and analysis*

Athena software was used to process XANES spectra (merging of replicate scans, energy calibration, background-removal, and normalization) and perform linear combination fits (Newville 2001; Ravel and Newville 2005). XRF maps were visualized and Mn fluorescence was quantified using DataViewer (Newville 2006). Spectra for a set of divalent (MnO), trivalent (Mn<sub>2</sub>O<sub>3</sub>), and tetravalent (MnO<sub>2</sub>) Mn-oxides were aligned across all dates and calibrated to a Mn foil standard set to  $E_0 = 6,537.7$  eV (Fig. A1). Edge energies were defined as the first peak after the pre-edge peak in the  $\mu(E)$  derivative spectrum (McKeown and Post 2001; Bunker 2010). MnO<sub>2</sub> was chosen to calibrate spectra collected on different dates due to its fully oxidized state. The energy shifts required to align the MnO<sub>2</sub> spectra ( $E_0 = 6,551.3 \pm 0.4$  eV) were applied to all samples for each collection date and were sufficient to align all Mn<sub>2</sub>O<sub>3</sub> ( $E_0 = 6,546.6 \pm 0.2$  eV) and MnO ( $E_0 = 6,543.2 \pm 0.3$  eV) spectra (Fig. A1).

Linear combination fits were performed between –20 eV and +30 eV around the Mn K-edge ( $E_0 = 6,537.7$  eV as reported for references) using the Combo method (Manceau et al. 2012). The Combo method yields information about the Mn oxidation state but is not used to quantify contributions from individual chemical species. We find this approach

useful for assessing oxidation states in environmental samples which may contain heterogeneous mixtures of compounds present in low abundance. Specifically, sample spectra were fit with 17 pure valence reference spectra (Fig. A2; Manceau et al. 2012) to determine the average oxidation state of Mn and relative fractions of Mn(II), Mn(III), and Mn(IV).

It was unclear whether mineral standards could be used to accurately calculate the oxidation state of Mn in organic samples, since reference oxide compounds bear little similarity with the free aqueous or organic-bound Mn found in plant tissues (Xu et al. 2009; Fernando et al. 2010). Thus, for comparison, spectra from vegetation samples were also fit with nine non-oxide spectra that included MnCl<sub>2</sub>, Mn(II)-oxalate, and Mn(III)-acetate solutions measured at APS, reported spectra for Mn(III) complexed with siderophores Rhizoferrin, Protochelin, and Desferrioxamine B (Harrington et al. 2012a, b), and a subset of the Manceau reference compounds (MnSO<sub>4</sub>(aq), Mn(II) sorbed to fungi, and MnPO<sub>4</sub>) (Fig. A2). The resulting data were highly similar to data derived from the original fits, and average deviations in the estimated proportions of Mn valence states calculated using the two libraries were small ( $\pm 4\%$ ). Thus, the inorganic and organic reference libraries were equally suited to quantify Mn oxidation state in the vegetation samples with minimal Mn(IV) ( $< 2\%$ ), and all results are reported using the reference spectra from Manceau et al. (2012).

The total fraction of each oxidation state was calculated as the sum of the fractions of individual components. All components were constrained to non-negative contributions. The relative qualities of linear combination fits were assessed using statistical outputs from the Athena software, including the reduced Chi square value ( $\chi_{\text{red}}^2$ ) reported here.  $\chi_{\text{red}}^2$  is equal to the sum of the squared differences between the data points and the model fit, divided by variance and degrees of freedom. Thus, lower reduced Chi square values indicate better model fits to the data.

## Results

### Soil chemistry

Mn concentrations in the bulk soil generally decreased from the soil surface ( $> 7,000 \mu\text{g g}^{-1}$ ) to near bedrock

( $< 1,500 \mu\text{g g}^{-1}$ ), consistent with previous studies (Fig. 1a) (Herndon et al. 2011). Manganese concentrations in sand-sized (Mn<sub>sand</sub>,  $\mu\text{g g}^{-1}$ ) and silt-sized (Mn<sub>silt</sub>,  $\mu\text{g g}^{-1}$ ) particles also generally decreased with depth, and Mn was contained principally in amorphous and crystalline oxides ( $\sim 86\%$ ) (Fig. 1; Table A1). On average across all depths, silt particles contained a higher proportion of Mn in amorphous oxides ( $55 \pm 6\%$ ) relative to sand particles ( $26 \pm 4\%$ ). In contrast, the sand particles contained a higher proportion of Mn in crystalline oxides ( $59 \pm 3\%$ ) relative to silt particles ( $37 \pm 4\%$ ). In both size fractions, the percent of Mn<sub>silt</sub> and Mn<sub>sand</sub> contained in amorphous oxides decreased while the percent contained in crystalline oxides increased with depth in the soil (Fig. 1e, f). Furthermore, sand particles contained more residual Mn ( $11 \pm 4\%$  of Mn<sub>sand</sub>) than silt particles ( $5.5 \pm 2.8\%$  of Mn<sub>silt</sub>). Given that the coarser sand particles are likely less weathered and more representative of bedrock than the silt particles, these results are consistent with an increase in Mn contained in bedrock-derived crystalline oxide and silicate minerals with depth.

XANES spectra for Mn in bulk soil varied with depth in a ridge soil profile and in a soil sample collected at the soil–bedrock interface in the valley floor (Fig. 2). In the ridge core, the absorption edges for the organic horizon and the deepest soil sample (16–22 cm) were shifted to slightly lower energies relative to the samples from 0 to 16 cm depth. Furthermore, a shoulder peak on the absorption edge at  $E = 6,557.6 \text{ eV}$  increased relative to the maximum absorption peak ( $E = 6,561.1 \text{ eV}$ ) with increasing depth. In the valley floor soil sample, two prominent shoulders were present at 6,552.0 and 6,557.6 eV. The increasing prominence of these shoulder peaks with depth indicates an increasing contribution of reduced Mn species.

Linear combination fits using the Combo method (Manceau et al. 2012) were used to calculate an average Mn oxidation state and quantify the relative fractions of Mn(II), Mn(III), and Mn(IV) in each sample (Table 1). The average oxidation state of Mn was  $+3.7$  in the organic horizon and decreased with increasing depth in the mineral soil from  $+3.9$  (0–16 cm) to  $+3.7$  (16–22 cm) to  $+3.5$  (62–66 cm). In the ridge core, the organic horizon and deepest mineral soil contained  $2\times$  more Mn(II) and  $\sim 3\text{--}6\times$  more Mn(III) than shallow mineral soils, which contained  $> 93\%$  Mn(IV). In the deepest sample from the

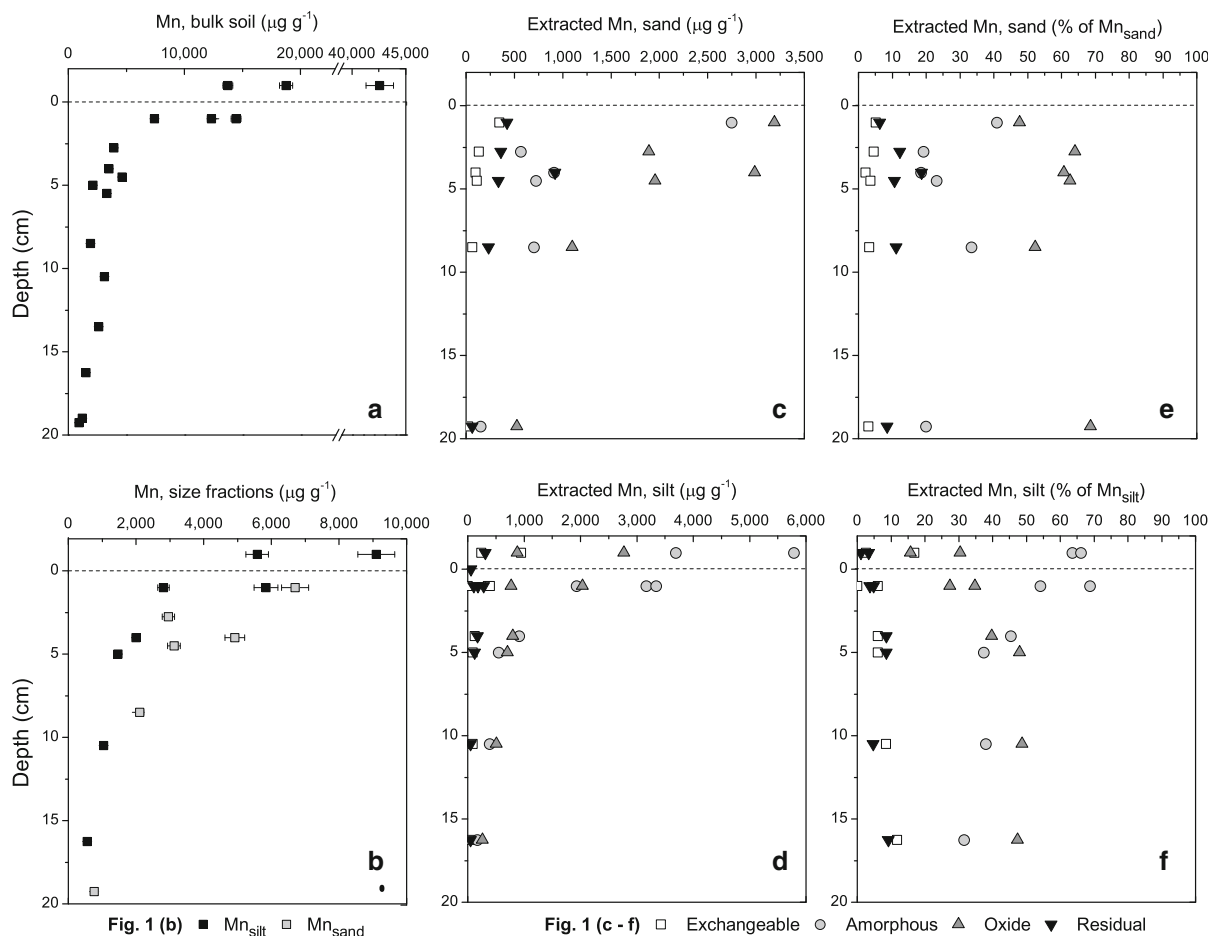


**Fig. 1** Manganese concentrations ( $\mu\text{g g}^{-1}$ ) in **a** bulk soil (including all particle sizes) and **b** sand and silt-sized soil particles ( $\text{Mn}_{\text{sand}}$  and  $\text{Mn}_{\text{silt}}$ , respectively) are plotted versus soil depth for samples reported in Table A1. **Panels (c-f)** show Mn

concentrations ( $\mu\text{g g}^{-1}$ ) and percentages of  $\text{Mn}_{\text{sand}}$  or  $\text{Mn}_{\text{silt}}$  contained in exchangeable, amorphous oxide, crystalline oxide, and residual phases for sand (**c, e**) and silt (**d, f**) particles

valley floor, Mn(III) comprised  $\sim 50\%$  of total Mn, followed by Mn(IV) (34 %) and Mn(II) (17 %).

Discrete Mn-rich regions were observed in  $\mu\text{XRF}$  images of soil grains collected near the soil surface (Fig. A3). In regions of low Mn, defined as  $<10\%$  of maximum Mn fluorescence, Mn was positively correlated with K, an element contained primarily in clay minerals. In contrast, Mn was not correlated with other elements in Mn-rich regions. Exceptionally Si-rich regions also showed poor correlation with other elements. These observations are consistent with mineral soil dominated by clay particles containing Si, K, Fe + minor Mn with some quartz particles (containing Si and O alone) and discrete Mn-rich particles or coatings.

## Vegetation

The Mn K-edge energy varied little amongst fresh green foliage, leaf litter, stem tissue and root tissue ( $E_0 = 6,547.0 \pm 0.7 \text{ eV}$ ;  $n = 31$ ). All spectra exhibited a steep absorption edge characteristic of organic-bound or aqueous Mn(II) (Fig. 3). Linear combination fits yielded an oxidation state of  $+2.2 \pm 0.1$  averaged over all vegetation samples with relative contributions of  $90 \pm 7\%$  Mn(II),  $10 \pm 7\%$  Mn(III), and  $<1\%$  Mn(IV). Amongst the vegetation samples, roots contained a higher proportion of Mn(II) ( $99 \pm 2\%$ ;  $n = 8$ ) relative to stems ( $91 \pm 2\%$ ;  $n = 3$ ) and green leaves ( $87 \pm 6\%$ ;  $n = 19$ ) (Table 1). There were no

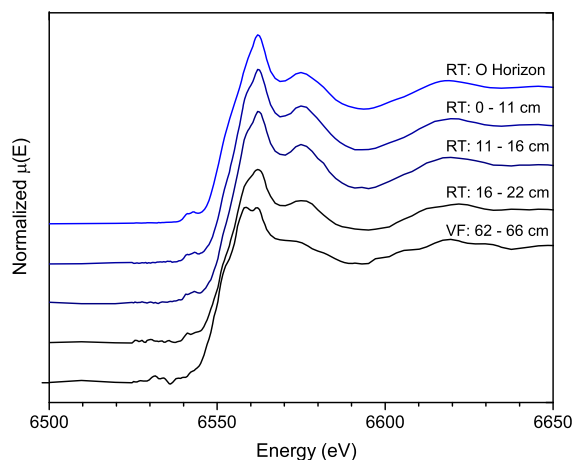


**Fig. 2** Mn K-edge XANES spectra for bulk soil samples collected from the Susquehanna Shale Hills Observatory (SSHCZO), including a complete ridge soil core (O horizon + mineral soil collected in depth increments of 0–11 cm, 11–16 cm, and 16–22 cm) and the soil–bedrock interface of a valley floor soil core (depth = 62–66 cm)

observed differences between oxidation states calculated from bulk and  $\mu$ XANES spectra.

### Foliage

Manganese concentrations in bulk foliar tissue were high ( $4,420 \pm 810 \mu\text{g g}^{-1}$ ,  $n = 12$ ) as measured on a subset of leaves used in this study. Dark spots on sampled leaves, a symptom of Mn toxicity, contained much higher levels of Mn than surrounding foliar tissue, as observed using x-ray fluorescence (Fig. 4). This feature was observed in leaves from both seedlings and mature trees and exhibited varied morphology (Fig. A4). Two Mn-rich dark spots on a

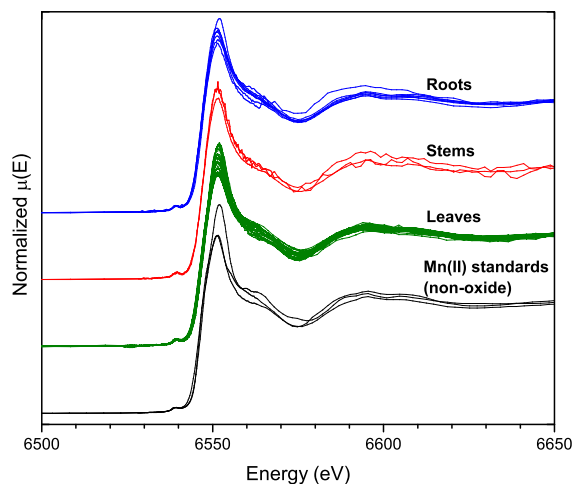


**Fig. 3** Mn K-edge XANES spectra for green leaf (green lines;  $n = 24$ ), stem (red lines;  $n = 3$ ), and root (blue lines;  $n = 7$ ) samples are similar to non-oxide Mn(II) standards including aqueous  $\text{MnCl}_2$ ,  $\text{MnSO}_4$ , and Mn(II) sorbed to fungi (black lines). (Color figure online)

red oak leaf were targeted for  $\mu$ XANES analysis to determine the chemical speciation of Mn in these regions relative to the bulk tissue. These spectra were distinct from other vegetation samples and indicated a high proportion of oxidized Mn for both spot 1 (46 % Mn(III) + 15 % Mn(IV);  $\chi_{\text{red}}^2 = 6.3 \times 10^{-5}$ ) and spot 2 (54 % Mn(III) + 15 % Mn(IV);  $\chi_{\text{red}}^2 = 7.5 \times 10^{-5}$ ). In contrast, a spectrum collected for a Mn-poor green area on the same leaf was similar to other vegetation samples (Fig. 4). Although these results indicate that the Mn-rich dark spots contain Mn(III), they do not distinguish between Mn bound to organic compounds or contained in oxides. Qualitative examination of Mn neighbor atoms (Fig. A5) indicated that

**Table 1** Manganese valence states for soil and plant samples determined by linear combination fits

	Average valence	Mn(II) (%)	Mn(III) (%)	Mn(IV) (%)	$\chi_{\text{red}}^2$ ( $\times 10^{-4}$ )
Soil samples					
O Horizon	3.7	10	9	80	7.9
RT08, 0–11 cm	3.9	5	2	94	6.2
RT08, 11–16 cm	3.9	4	4	93	4.8
RT08, 16–22 cm	3.7	8	19	73	6.1
VF08, 62–66 cm	3.5	17	49	34	15.0
Plant samples					
Green foliage ( $\pm 6$ %)	2.2	87	13	0	12.0
Roots ( $\pm 2$ %)	2.1	99	1	0	1.5
Stems ( $\pm 2$ %)	2.1	91	8	0	6.3
Leaf litter	2.1	87	13	0	17.1

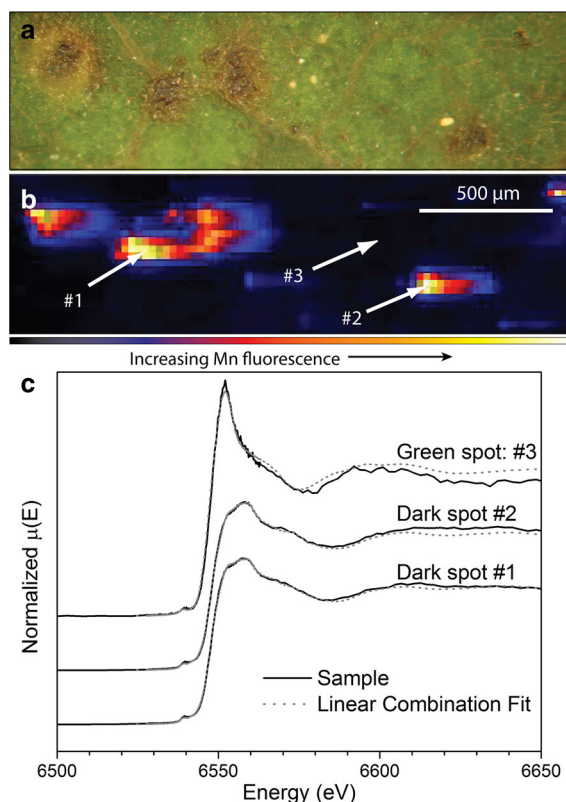


**Fig. 4** Optical (a) and corresponding XRF (b) images of a leaf from a mature red oak at SSHCZO. In the XRF image, pixels with warm colors correspond to high Mn fluorescence values and indicate regions of high Mn concentrations. c  $\mu$ XANES spectra from two Mn-rich dark spots on foliage (spots #1 and #2) are distinct from both the bulk leaf spectrum and a  $\mu$ XANES spectrum taken from the green leaf tissue (spot #3). The model outputs of linear combination fits, shown as *dotted grey lines*, are most consistent with 38 % Mn(II) + 46 % Mn(III) + 15 % Mn(IV) (spot #1), 31 % Mn(II) + 54 % Mn(III) + 15 % Mn(IV) (spot #2), and 71 % Mn(II) + 29 % Mn(III) (spot #3)

spectra from the dark spots did not exhibit the Mn–Mn scattering patterns observed for Mn-oxides nor Mn–P scattering patterns observed by McNear and Kupper (2014) and were instead more similar to organic-Mn(III) chelates described by Harrington et al. (2012a, b); however, more detailed analyses are required to confirm this observation.

In one additional leaf sample from a red oak seedling,  $\mu$ XANES spectra were taken on two Mn-rich dark spots of differing Mn intensity (Fig. A6). The less Mn-rich spot was consistent with 100 % Mn(II) ( $\chi^2_{\text{red}} = 3.1 \times 10^{-4}$ ) while the more Mn-rich spot exhibited a higher energy absorption peak consistent with contribution from Mn(IV) ( $\chi^2_{\text{red}} = 4.0 \times 10^{-4}$ ). However, some spectra

obtained from Mn-rich regions were similar to the bulk vegetation and did not indicate the presence of oxidized compounds (Fig. A7). The differences amongst these spectra suggest that the extent of Mn oxidation may vary during Mn accumulation.

#### Woody vegetation

Manganese in stems and roots was dominantly present as Mn(II) and enriched in distinct regions. As observed in a cross-section of a *Q. prinus* stem, Mn was enriched in phloem tissue relative to xylem tissue (Fig. 5). Spectra taken from the Mn-rich phloem, Mn-poor xylem, and the outer rim of the stem were indistinguishable and consistent with  $12 \pm 2$  % Mn(III) and  $88 \pm 2$  % Mn(II). In coarse roots with woody tissue, Mn was concentrated in the outer portion of the root, exhibiting a Mn-rich band in what is likely phloem tissue (e.g. Fig. 5), although resolution of the image makes determination of the exact tissue difficult. In fine roots with no woody tissue, Mn was concentrated in the inner portion of the root, similar to K, and opposite to Ca (Fig. A8). For roots, spectra from 8  $\mu$ XANES spots were consistent with  $99 \pm 2$  % Mn(II) and  $1 \pm 2$  % Mn(III) (Table 1). The abundance of Mn(II) in all portions of the root tissue indicate that Mn-oxidation did not occur in or near the roots in these red oak seedlings. Rather, average Mn oxidation states increased from roots to stems to the leaves.

#### Decomposing vegetation

We next evaluated XANES spectra for decomposing vegetation samples that included: (1) leaves and roots that were analyzed while fresh and reanalyzed after 6 months of decomposition in the laboratory, and (2) leaf litter buried in field or greenhouse pot soils for 7–9 weeks. We compared these spectra to green leaf, leaf litter, and organic and mineral soils as previously characterized (Figs. 2 and 3), and found that spectra from the decomposing samples were intermediate between green leaves and the mineral soil (Fig. 6). In contrast to fresh vegetation (90 % Mn(II) + 10 % Mn(III)), leaf samples decomposed for six months contained as little as 40 % Mn(II) and up to 38 % Mn(III) and 23 % Mn(IV). Similarly, a root sample experienced a 39 % decrease in Mn(II) and a 43 % increase in Mn(IV) during decomposition.

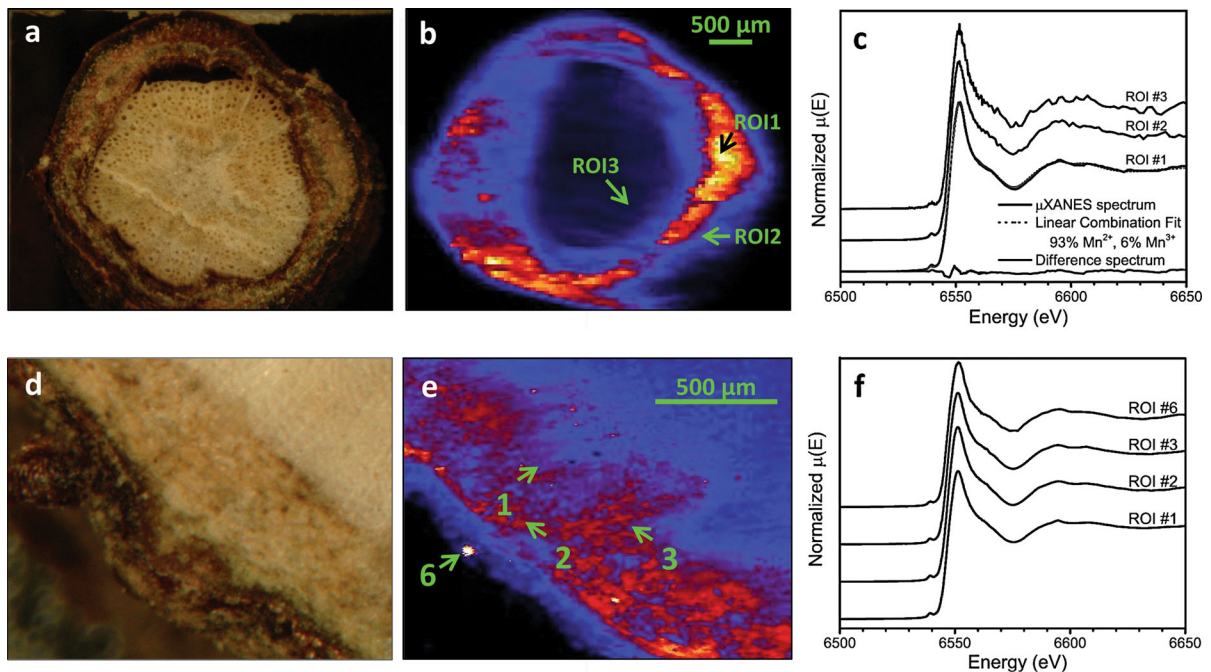


**Fig. 5** From left to right: optical image, Mn XRF image,  $\mu$ XANES Mn spectra. **Panel a** shows the cross-section of a stem (diameter = 4 mm) from a mature chestnut oak. **b** Mn is concentrated in the outer portion of the stem tissue while the inner xylem tissue contains low levels of Mn. **c** Three  $\mu$ XANES spectra taken from across the stem are highly similar, and a

linear combination fit to ROI #1 (dotted grey line) indicates a high proportion of Mn was present as Mn(II). **Panel d** shows the edge of a cross-section of a large woody root (~8 mm diameter) from a red oak seedling. **e** Mn is concentrated in the outer part of the root. **f**  $\mu$ XANES spectra from the root (spots 1, 2, 3 and 6 on Fig. 5e) are highly similar and consistent with Mn(II)

Similar results were observed for leaf litter samples that were analyzed after burial in soils for 7–9 weeks. In total, nine  $\mu$ XANES spots were obtained from buried wells containing crushed leaf litter (Fig. A9a). Of those nine, six spectra were taken from three wells buried in greenhouse pots, while three spectra were taken from two wells buried in the field. Leaf litter buried in greenhouse soils contained 84–90 % Mn(II) and 10–16 % Mn(III), suggesting only slight alteration after 9 weeks. In contrast, leaf litter buried in the field soils contained high levels of oxidized Mn after 7 weeks. Specifically, two spectra taken on Mn hot spots ( $Mn/I_0 = 0.74$  and  $1.09$ ) had more Mn(III) (35–36 %) and Mn(IV) (31–43 %) relative to a Mn-poor spot ( $Mn/I_0 = 0.02$ ) which contained only 27 % Mn(III) and 9 % Mn(IV).

## Discussion

Changes in Mn XANES with depth in the soil profile were consistent with a mixing of different pools of Mn.

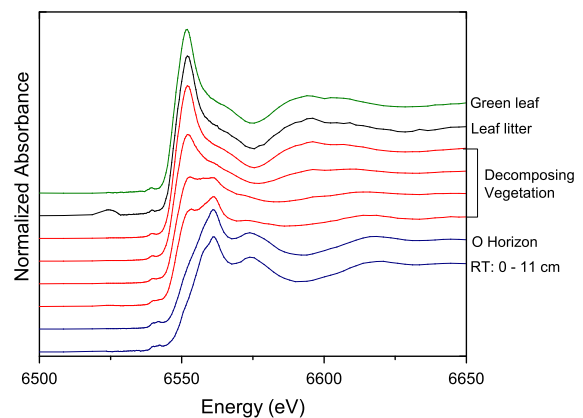


**Fig. 6** Spectra of normalized  $\mu(E)$  for bulk soil and vegetation samples are stacked from top to bottom as fresh vegetation (green), leaf litter (black) decomposing vegetation (red), and soil samples (blue) and exhibit the transition from samples dominated by organic and aqueous Mn(II) to samples dominated by Mn(III/IV)-oxides. (Color figure online)

In particular, the proportions of Mn(II) + Mn(III) present in the mineral soil increased relative to Mn(IV) with increasing depth (Fig. 7). In previous research, Jin

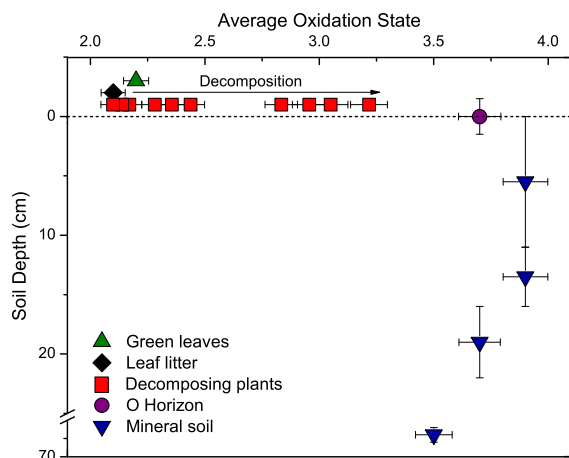


**Fig. 7** The average oxidation states of Mn in the soil–plant system, determined using linear combination fits to XANES spectra, are plotted versus depth in a soil profile. Depths for leaf and decomposing vegetation samples are arbitrarily placed <0 cm to indicate their position above the mineral soil surface ( $=0$  cm). Error bars indicate either the sampling depth interval ( $y$ -error) or the standard deviation of valence state measured on Mn-oxide calibration standards ( $x$ -error)

et al. (2010) documented that ridge soils at SSHCZO contain 38–41 wt% clays as illite, kaolinite, and mixed chlorite-vermiculite phases. In comparison, the deepest soils from the valley floor contain 63 wt% clays as illite and chlorite. Using that information, we suggest that Mn in soils near the bedrock interface was derived at least partially from protolith clay minerals while Mn in the surface mineral soils was present as Mn(III)/Mn(IV)-oxides. In fact, the Mn XANES spectrum for the deepest soil sample exhibited the same double peak and prominent shoulder previously observed for Mn in illite (Huggins et al. 1997). Additionally, we conclude that the organic horizon contained predominately Mn(III)/(IV)-oxides mixed with Mn(II) contained in organic matter. No Mn-oxide minerals have been directly identified by XRD in the soils, likely due to their relatively low abundance (<1.5 wt%) and poorly-crystalline structure (Jin et al. 2010).

Changes in the proportions of Mn in amorphous and crystalline oxides with depth suggest different pathways of Mn-oxide formation. Initial products of Mn(II) oxidation are amorphous to poorly crystalline oxides, and crystallinity increases with aging (Tebo et al. 2004; Cui et al. 2010; Santelli et al. 2011). If all Mn oxides in the soil formed during soil weathering, we would expect more amorphous oxides in the less weathered soil at depth and more crystalline oxides in

the highly weathered soil near the land surface. However, the high proportion of Mn in the amorphous fraction near the soil surface indicates recent formation relative to the crystalline oxides at depth. We propose that Mn-oxides deep in the soil formed as Mn(II) ions leached from silicate minerals during weathering and were oxidized, forming crystalline oxides over the long timescales of soil formation (millennia to tens of millennia). In contrast, amorphous Mn-oxides at the soil surface likely formed during the oxidation of Mn(II) contained in organic matter over the short timescales of decomposition (years to decades). In this study, we observed that Mn(II) contained in decomposing leaf litter was precipitated as Mn(III)/(IV)-oxides within 6 months.

However, secondary mineral formation cannot account for the net enrichment of Mn in the soil profiles calculated by Herndon et al. (2011). Addition of Mn to these soil profiles was previously attributed to atmospheric inputs from industrial sources and inferred to have consisted of aqueous Mn and/or particulate Mn-oxide species. Previous researchers report emissions of both soluble Mn sulfates and phosphates and insoluble  $Mn_3O_4$  and  $MnO_2$  from anthropogenic sources (U.S. Environmental Protection Agency 1984; Zayed et al. 1999; Ressler et al. 2000). Thus, Mn may have been input to the surface soils as Mn-oxides, or Mn-oxides may have precipitated in the soil following inputs of soluble Mn. Although the proportion of Mn present as crystalline oxides decreases towards the surface, the total concentration increases, and we infer that the crystalline Mn-oxides near the soil surface were input as particles during a period of heavy industrial inputs. Due to similarities in mineralogy, we cannot distinguish between Mn-oxide particles input through industrial deposition and Mn-oxides formed during decomposition of plant biomass near the soil surface. However, Mn that is leached from the atmospherically-deposited Mn particles may be accumulated by vegetation and reprecipitated as biogenic Mn-oxides. Thus, industrial inputs are still the ultimate source of Mn at the soil surface. The uptake and storage of aqueous Mn(II) by vegetation and eventual immobilization as Mn-oxides in the soil likely slows the removal of Mn contamination from soils into rivers.

Similar to previous studies, we found that Mn in the plant biomass was predominantly aqueous or organic-bound Mn(II) (Xu et al. 2009; Fernando et al. 2010).

Despite the demonstrated immobility of Mn in phloem sap (Hocking 1980; Riesen and Feller 2005), we observed high levels of Mn in phloem tissues relative to the xylem. This observation also does not contradict previous studies, but rather suggests that Mn is utilized for biochemical processes in the living phloem cells and merely transported through dead xylem cells without storage. Although many plant species are able to oxidize Mn in the root zone (Horiguchi 1987), we observed no evidence of Mn oxidation in these root samples. Rather, the average Mn oxidation state increased from root to leaf. While the particular organic moiety binding Mn may differ amongst these compartments, Mn K-edge XANES could not satisfactorily distinguish among them.

Our analysis of decomposing leaves and roots revealed that Mn in these tissues consisted largely of organic Mn(II) that transformed to Mn(III/IV)-oxides in the soil upon decomposition (Fig. 7). XANES spectra for Mn in green leaves and leaf litter were similar; thus, we infer that oxidation of the Mn in plant tissues did not commence until after litterfall. Significant alteration of Mn in leaf tissue occurred within 2–6 months of the initiation of decomposition, as measured in our laboratory and field decomposition experiments (Figs. 6 and A9a). Spontaneous abiotic precipitation of Mn-oxides is not expected in aqueous solution at the low pH conditions present in these soils (Tebo et al. 2004). Rather, bacteria and fungi are largely responsible for Mn-oxide formation in the environment, and fungi may be more important than bacteria in many terrestrial systems (Thompson et al. 2005; Santelli et al. 2010). Both bacteria and fungi catalyze the production of Mn-oxide minerals that yield XANES spectra similar to those obtained for the organic horizon and surface soil in this study (Bargar et al. 2005; Miyata et al. 2006; Santelli et al. 2011).

Finally, the leaves analyzed in this study often exhibited dark spots, a symptom of Mn toxicity. These spots were found to be Mn-rich relative to the surrounding leaf tissue and contained varying degrees of Mn(II) and Mn(III)-organic complexes. Previous studies have attributed the formation of these dark spots to the accumulation of phenolic compounds and/or oxidized Mn deposits (Horiguchi 1987; Broadhurst et al. 2009), but the presence of Mn(III) has only recently been identified in leaves of a metal hyperaccumulating herb (McNear and Kupper 2014). The Mn(III) ion is unstable in aqueous solution and only

persists as a complex with strong organic ligands (Duckworth and Sposito 2005; Trouwborst et al. 2006; Madison et al. 2011), and our observations of foliar Mn(III) are also consistent with the presence of organic-Mn(III) complexes. It is possible that Mn(III) was produced in the leaves via the oxidation of excess Mn(II) by superoxides (Gonzalez et al. 1998; St. Clair et al. 2005), similar to a proposed mechanism for bacterial production of Mn(III) during Mn-oxide formation (Tebo et al. 2004; Learman et al. 2011a, b). In leaves, abundant organic chelates are available to stabilize Mn(III), slowing both rates of reduction to Mn(II) and transformation into Mn-oxides.

## Conclusions

The fate and transport of industrial contaminants through the environment depend on their interactions with soil minerals and biota. In previous studies, we suggested that vegetation accumulates large quantities of Mn from the soil, storing it in biomass and organic matter and attenuating its release into rivers over time. Here, we demonstrated that Mn that is taken up by vegetation is taken up as Mn(II) species that are then rapidly oxidized as vegetation is decomposed in the soil. A small portion of foliar Mn is present as Mn(III)-organic complexes in distinct Mn-rich spots on the leaves, the formation of which we hypothesize is due to superoxide oxidation mechanisms previously only observed for bacteria and fungi in the soil. Upon senescence and leaf fall in autumn, the Mn stored in leaves is released but rapidly immobilized during litter decomposition. We propose that Mn can be preferentially retained in soils relative to other elements due to this process of uptake and immobilization. Namely, vegetation takes up the majority of Mn that is solubilized in the soil within the rooting zone and drastically reduces the quantity that can be leached from the soil profile. The Mn that is taken up into plant biomass exists mostly as aqueous and organic Mn(II) compounds that are immobilized as Mn(III)/(IV)-oxides during decomposition. The recurring cycle of solubilization from the solid-phase followed by uptake into vegetation and subsequent immobilization effectively retains Mn within the soil–plant system.

**Acknowledgments** This study was supported by National Science Foundation grant EAR #1052614 to SLB, the NSF

Susquehanna Shale Hills Critical Zone Observatory grant EAR #0725019 to C. Duffy (Penn State), and NSF grant CHE #0431328 to SLB. The authors particularly acknowledge the help of Matthew Newville (GSECARS) and Dale Brewe (PNC/XSD) at APS and Timothy Fischer for scientific support at the beamlines, and Katie Gaines, Jim Savage, and Jane Wubbels for leaf collection at SSHCZO. Portions of this work ( $\mu$ XRF and  $\mu$ XANES) were performed at GeoSoilEnviroCARS (Sector 13), Advanced Photon Source (APS), Argonne National Laboratory. GeoSoilEnviroCARS is supported by the NSF—Earth Sciences (EAR-1128799) and DOE—Geosciences (DE-FG02-94ER14466). Use of the APS was supported by the U. S. Department of Energy Office of Science, Office of Basic Energy Sciences, under Contract No. DE-AC02-06CH11357. Other portions of this work (bulk XANES) were performed at PNC/XSD facilities. PNC/XSD facilities at the APS, and research at these facilities, are supported by the US DOE—Basic Energy Sciences, a Major Resources Support grant from NSERC, the University of Washington, Simon Fraser University and the Advanced Photon Source. Use of the Advanced Photon Source, an Office of Science User Facility operated for the U.S. DOE Office of Science by Argonne National Laboratory, was supported by the U.S. DOE under Contract No. DE-AC02-06CH11357.

## References

- Andrews DM, Lin H, Zhu Q, Jin L, Brantley SL (2011) Hot spot and hot moments of dissolved organic carbon export and soil organic carbon storage in the Shale Hills catchment. *Vadose Zone J* 10:943–954
- Archibald FS, Fridovich I (1982) The scavenging of superoxide radical by manganous complexes: in vitro. *Arch Biochem Biophys* 214(2):452–463
- Bargar JR, Webb SM, Tebo BM (2005) EXAFS, XANES and In-Situ SR-XRD characterization of biogenic manganese oxides produced in sea water. *Phys Scr* T115:888–890
- Berg B, Steffen KT, McLaugherty C (2007) Litter decomposition rate is dependent on litter Mn concentrations. *Biogeochemistry* 82:29–39
- Blamey FPC, Joyce DC, Edwards DG, Asher CJ (1986) Role of trichomes in sunflower tolerance to manganese toxicity. *Plant Soil* 91:171–180
- Brantley SL, Lebedeva M (2011) Learning to read the chemistry of the regolith to understand the Critical Zone. *Ann Rev Earth Planet Sci* 39:387–416
- Broadhurst CL, Tappero RV, Mangel TK, Erbe EF, Sparks DL, Chaney RL (2009) Interaction of nickel and manganese in accumulation and localization in leaves of the Ni hyper-accumulators *Alyssum murale* and *Alyssum corsicum*. *Plant Soil* 314:35–48
- Bunker G (2010) Introduction to XAFS: a practical guide to X-ray absorption fine structure spectroscopy, 1st edn. Cambridge University Press, Cambridge, MA
- Cui H, Liu F, Feng X, Tan W, Wang MK (2010) Aging promotes todorokite formation from layered manganese oxide at near-surface conditions. *J Soils Sediments* 10:1540–1547
- Duckworth OW, Sposito G (2005) Siderophore-manganese(III) interactions II. Manganite dissolution promoted by desferrioxamine B. *Environ Sci Technol* 39:6045–6051
- Eickhorst T, Tippkötter R (2008) Detection of microorganisms in undisturbed soil by combining fluorescence in situ hybridization (FISH) and micropedological methods. *Soil Biol Biochem* 40:1284–1293
- Fernando DR, Mizuno T, Woodrow IE, Baker AJM, Collins RN (2010) Characterization of foliar manganese (Mn) in Mn (hyper)accumulators using X-ray absorption spectroscopy. *New Phytol* 188:1014–1027
- Gonzalez A, Lynch JP (1999) Subcellular and tissue Mn compartmentation in bean leaves under Mn toxicity stress. *Aust J Plant Physiol* 26:811–822
- Gonzalez A, Steffen K, Lynch J (1998) Light and excess manganese. Implications for oxidative stress in common bean. *Plant Physiol* 118:493–504
- Harrington JM, Parker DL, Bargar JR, Jarzecki AA, Tebo BM, Sposito G, Duckworth O (2012a) Structural dependence of Mn complexation by siderophores: donor group dependence on complex stability and reactivity. *Geochim Cosmochim Acta* 88:106–119
- Harrington JM, Bargar JR, Jarzecki AA, Roberts JG, Sombers LA, Duckworth OW (2012b) Trace metal complexation by the triscatecholate siderophore protochelin: structure and stability. *Biometals* 25:393–412
- Herndon EM (2012) Biogeochemistry of manganese contamination in a temperate forested watershed. PhD Dissertation, The Pennsylvania State University
- Herndon EM, Brantley SL (2011) Movement of manganese contamination through the critical zone. *Appl Geochem* 26:S40–S43
- Herndon EM, Jin L, Brantley SL (2011) Soils reveal widespread manganese enrichment from industrial inputs. *Environ Sci Technol* 45:241–247
- Hocking PJ (1980) The Composition of phloem exudate and xylem sap from tree tobacco (*Nicotiana glauca* Grah.). *Ann Bot* 45:633–643
- Hofrichter M (2002) Review: lignin conversion by manganese peroxidase (MnP). *Enzym Microb Technol* 30:454–466
- Horiguchi T (1987) Mechanism of manganese toxicity and tolerance of plants. *Soil Sci Plant Nutr* 33:595–606
- Horsley SB, Long RR, Bailey SW, Hallett RA, Hall TJ (2000) Factors associated with the decline disease of sugar maple on the Allegheny Plateau. *Can J For Res* 30:1365–1378
- Huggins FE, Srikantapura S, Parekh BK, Blanchard L, Robertson JD (1997) XANES spectroscopic characterization of selected elements in deep-cleaned fractions of Kentucky No. 9 Coal. *Energy Fuels* 11:691–701
- Jin L, Ravella R, Ketchum B, Bierman PR, Heaney P, White T, Brantley SL (2010) Mineral weathering and elemental transport during hillslope evolution at the Susquehanna/Shale Hills Critical Zone Observatory. *Geochim Cosmochim Acta* 74:3669–3691
- Jobby EG, Jackson RB (2004) The uplift of soil nutrients by plants: biogeochemical consequences across scales. *Ecology* 85:2380–2389
- Kabata-Pendias A, Pendias H (2001) Trace elements in soils and plants, 3rd edn. CRC Press LLC, Boca Raton
- Kogelmann WJ, Sharpe WE (2006) Soil acidity and manganese in declining and nondeclining sugar maple stands in Pennsylvania. *J Environ Qual* 35:433–441

- Learman DR, Wankel SD, Webb SM, Martinez N, Madden AS, Hansel CM (2011a) Coupled biotic–abiotic Mn(II) oxidation pathway mediates the formation and structural evolution of biogenic Mn oxides. *Geochim Cosmochim Acta* 75:6048–6063
- Learman DR, Voelker BM, Vazquez-Rodriguez AI, Hansel CM (2011b) Formation of manganese oxides by bacterially generated superoxide. *Nat Geosci* 4:95–98
- Learman DR, Voelker BM, Madden AS, Hansel CM (2013) Constraints on superoxide mediated formation of manganese oxides. *Front Microbiol* 4:262
- Ma L, Chabaux F, Pelt E, Blaes E, Jin L, Brantley SL (2010) Regolith production rates calculated with uranium-series isotopes at Susquehanna/Shale Hills Critical Zone Observatory. *Earth Planet Sci Lett* 297:211–225
- Madison AS, Tebo Bradley M, Luther GW (2011) Simultaneous determination of soluble manganese(III), manganese(II) and total manganese in natural (pore)waters. *Talanta* 84:374–381
- Manceau A, Marcus MA, Grangeon S (2012) Determination of Mn valence states in mixed-valence manganates by XANES spectroscopy. *Am Mineral* 97:816–827
- McKeown D, Post J (2001) Characterization of manganese oxide mineralogy in rock varnish and dendrites using X-ray absorption spectroscopy. *Am Mineral* 86:701–713
- McNear DH, Kupper JV (2014) Mechanisms of trichome-specific Mn accumulation and toxicity in the Ni hyperaccumulator *Alyssum murale*. *Plant Soil* 377:407–422
- McNear DH, Peltier E, Everhart J, Chaney RL, Sutton S, Newville M, Rivers M, Sparks DL (2005) Application of quantitative fluorescence and absorption-edge computed microtomography to image metal compartmentalization in *Alyssum murale*. *Environ Sci Technol* 39:2210–2218
- Miyata N, Tani Y, Maruo K, Tsuno H, Sakata M, Iwahori K (2006) Manganese(IV) oxide production by *Acremonium* sp. strain KR21-2 and extracellular Mn(II) oxidase activity. *Appl Environ Microbiol* 72:6467–6473
- Newville M (2001) EXAFS analysis using FEFIT and FEFIT. *J Synchrotron Radiat* 8:96–100
- Newville M. (2006) DataViewer. <http://cars.uchicago.edu/~newville/dataviewer>
- Nriagu J, Pacyna J (1988) Quantitative assessment of worldwide contamination of air, water and soils by trace metals. *Nature* 333:134–139
- Nunan N, Ritz K, Crabb D, Harris K, Wu K, Crawford JW, Young IM (2001) Quantification of the in situ distribution of soil bacteria by large-scale imaging of thin sections of undisturbed soil. *FEMS Microbiol Ecol* 36:67–77
- Oh N-H, Richter DD (2005) Element translocation and loss from three highly weathered soil-bedrock profiles in the southeastern United States. *Geoderma* 126:5–25
- Pacyna JM, Pacyna EG (2001) An assessment of global and regional emissions of trace metals to the atmosphere from anthropogenic sources worldwide. *Environ Rev* 9:269–298
- Ravel B, Newville M (2005) Athena, Artemis, and Hephaestus: Data analysis for x-ray absorption spectroscopy using IF-EFFIT. *J Synchrotron Radiat* 12:537–541
- Ressler T, Wong J, Roos J, Smith IL (2000) Quantitative speciation of mn-bearing particulates emitted from autos burning (methylcyclopentadienyl)manganese tricarbonyl-added gasolines using xanes spectroscopy. *Environ Sci Technol* 34:950–958
- Riesen O, Feller U (2005) Redistribution of nickel, cobalt, manganese, zinc, and cadmium via the phloem in young and maturing wheat. *J Plant Nutr* 28:421–430
- Santelli CM, Pfister DH, Lazarus D, Sun L, Burgos WD, Hansel CM (2010) Promotion of Mn(II) oxidation and remediation of coal mine drainage in passive treatment systems by diverse fungal and bacterial communities. *Appl Environ Microbiol* 76:4871–4875
- Santelli CM, Webb SM, Dohnalkova AC, Hansel CM (2011) Diversity of Mn oxides produced by Mn(II)-oxidizing fungi. *Geochim Cosmochim Acta* 75:2762–2776
- Schulze D, McCay-Buis T, Sutton SR, Huber D (1995) Manganese oxidation states in *Gaeumannomyces*-infested wheat rhizospheres probed by micro-XANES spectroscopy. *Phytopathology* 85:990–994
- St. Clair SB, Carlson JE, Lynch Jonathan P (2005) Evidence for oxidative stress in sugar maple stands growing on acidic, nutrient imbalanced forest soils. *Oecologia* 145:258–269
- Suarez D, Langmuir D (1976) Heavy metal relationships in a Pennsylvania soil. *Geochim Cosmochim Acta* 40:589–598
- Tebo BM, Bargar JR, Clement BG, Dick GJ, Murray KJ, Parker D, Verity R, Webb SM (2004) Biogenic manganese oxides: properties and mechanisms of formation. *Annu Rev Earth Planet Sci* 32:287–328
- Thompson I, Huber DM, Guest C, Schulze DG (2005) Fungal manganese oxidation in a reduced soil. *Environ Microbiol* 7:1480–1487
- Tippkötter R, Ritz K (1996) Evaluation of polyester, epoxy and acrylic resins for suitability in preparation of soil thin sections for in situ biological studies. *Geoderma* 69:31–57
- Trouwborst RE, Clement BG, Tebo BM, Glazer BT, Luther GW (2006) Soluble Mn(III) in suboxic zones. *Sci (New York, N.Y.)* 313:1955–1957
- U.S. Environmental Protection Agency (1984) Health assessment document for manganese. Cincinnati, Ohio
- Webb SM, Dick GJ, Bargar JR, Tebo BM (2005) Evidence for the presence of Mn(III) intermediates in the bacterial oxidation of Mn(II). *Proc Nat Acad Sci* 102:5558–5563
- White PJ (2012) Long-distance Transport in the Xylem and Phloem. In Marschner's Mineral Nutrition of Higher Plants Elsevier Ltd. pp. 49–70
- Wubbels JK (2010) Tree species distribution in relation to stem hydraulic traits and soil moisture in a mixed hardwood forest in central Pennsylvania. Master's Thesis, The Pennsylvania State University
- Xu X, Shi J, Chen X, Chen Y, Hu T (2009) Chemical forms of manganese in the leaves of manganese hyperaccumulator *Phytolacca acinosa* Roxb. (Phytolaccaceae). *Plant Soil* 318:197–204
- Zayed J, Hong B, L'esperance G (1999) Characterization of Manganese-Containing Particles Collected from the Exhaust Emissions of Automobiles Running with MMT Additive. *Environ Sci Technol* 33:3341–3346